

Regional energy budget control of the intertropical convergence zone and application to mid-Holocene rainfall

William R. Boos^{1*} and Robert L. Korty²

Shifts in the latitude of the intertropical convergence zone—a region of intense tropical rainfall—have often been explained through changes in the atmospheric energy budget, specifically through theories that tie rainfall to meridional energy fluxes. These quantitative theories can explain shifts in the zonal mean, but often have limited relevance for regional climate shifts, such as a period of enhanced precipitation over Saharan Africa during the mid-Holocene. Here we present a theory for regional tropical rainfall shifts that utilizes both zonal and meridional energy fluxes. We first identify a qualitative link between zonal and meridional energy fluxes and rainfall variations associated with the seasonal cycle and the El Niño/Southern Oscillation. We then develop a quantitative theory based on these fluxes that relates atmospheric energy transport to tropical rainfall. When applied to the orbital configuration of the mid-Holocene, our theory predicts continental rainfall shifts over Africa and Southeast Asia that are consistent with complex model simulations. However, the predicted rainfall over the Sahara is not sufficient to sustain vegetation at a level seen in the palaeo-record, which instead requires an additional large energy source such as that due to reductions in Saharan surface albedo. We thus conclude that additional feedbacks, such as those involving changes in vegetation or soil type, are required to explain changes in rainfall over Africa during the mid-Holocene.

The vertically integrated atmospheric energy budget has become a widely used means of understanding tropical rainfall changes. It was first used 30 years ago to relate time-mean tropospheric ascent, and thus rainfall, to the humidity distribution and to energy fluxes through the top and bottom of the tropical atmosphere¹. More recently, this energy budget was shown to link meridional intertropical convergence zone (ITCZ) shifts with remote, high-latitude thermal forcings such as those in the last deglaciation^{2–4}. Tropical rainfall shifts are linked to remote energy sources by the Hadley circulation, which transports energy meridionally away from its ascending branch (the ITCZ) in the same direction as upper-tropospheric winds, balancing the net tropical radiative energy source and the net high-latitude sink. Given an anomalous energy source imposed in one hemisphere, an anomalous Hadley circulation can restore local energy balance; the circulation anomaly constitutes an ITCZ shift toward the hemisphere containing the positive anomalous energy source⁵.

These ideas hold quantitatively, with zonal mean ITCZ position correlating with zonal mean meridional atmospheric energy transport (AET). In the observed seasonal cycle and in global climate model (GCM) simulations of the mid-Holocene and Last Glacial Maximum, the ITCZ shifts northward by roughly 3° latitude for every petawatt of southward cross-equatorial AET⁶. This scaling, which has been generalized by linearizing AET anomalies about the modern climate state⁷, constitutes a theory for ITCZ latitude⁸. However, this zonal mean theory has limited relevance to regional changes: the zonal mean ITCZ was estimated to shift less than 1° latitude between today and either the Last Glacial Maximum or mid-Holocene, while climate proxies indicate regional ITCZ (we use ITCZ synonymously with regions of intense time-mean tropical rainfall) displacements larger than 5° latitude⁹. Taylor expansions of cross-equatorial AET at a given longitude have been used to

diagnose local meridional ITCZ shifts¹⁰, but this requires knowing the cross-equatorial AET and gives no information on zonal ITCZ shifts. Thus, we lack a quantitative theory to explain even the order of magnitude of regional ITCZ shifts produced by an arbitrary energy source.

This lack of theory has been particularly troubling for the mid-Holocene, 6 kyr ago. Precipitation proxies indicate that the Sahara was wetter when the boreal summer northward insolation gradient was enhanced in the mid-Holocene^{11–14}, but simulations by three generations of palaeoclimate models consistently underpredict the northward expansion of African rainfall^{15–17}. Saharan rainfall consistent with proxies can be simulated when Saharan surface properties are changed to those of a grassland^{18–21}, but this result relies entirely on integrating complex climate models. The zonal mean atmospheric energy budget was invoked to explain this response to albedo variations²², but that framework provides only qualitative understanding of regional Saharan change. A quantitative theory for the regional response to orbital forcing remains a key missing component in climate studies.

Here we demonstrate that zonal energy transports can be just as important as meridional transports in their association with regional rainfall. We review this association qualitatively for the El Niño/Southern Oscillation (ENSO), and then develop a quantitative theory for mid-Holocene precipitation shifts. To be clear, any theory for ITCZ shifts must be augmented by theories for changes in precipitation intensity and spatial structure; these are expected to be important for the response to global warming²³ or cooling²⁴, in contrast to the response to orbital precession²⁵.

The importance of zonal energy fluxes

ENSO is a prominent mode of climate variability, yet has a small effect on zonal mean precipitation and AET. Zonal mean rainfall

¹Department of Geology and Geophysics, Yale University, New Haven, Connecticut 06511, USA. ²Department of Atmospheric Sciences, Texas A&M University, College Station, Texas 77843, USA. *e-mail: billboos@alum.mit.edu

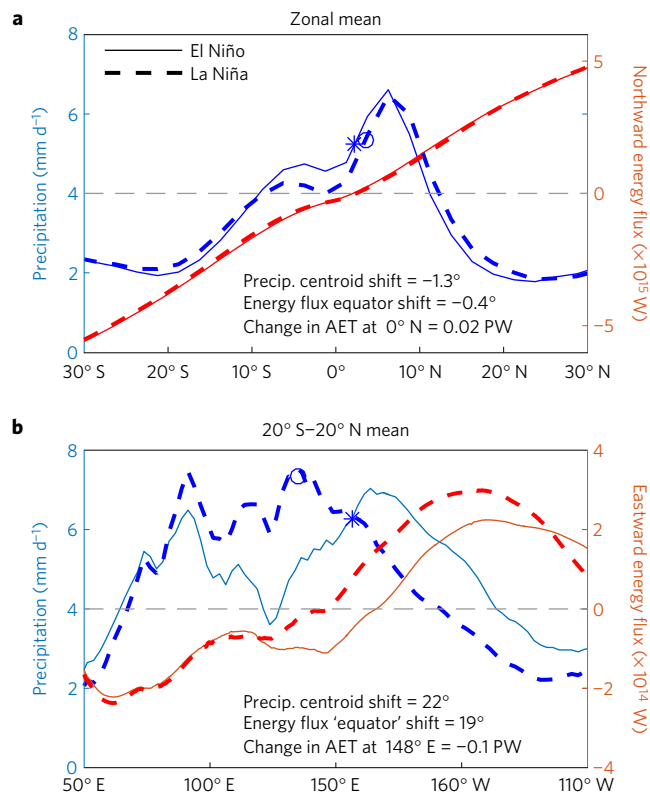


Figure 1 | One-dimensional perspective on the importance of zonal energy fluxes during the El Niño/Southern Oscillation. **a**, Zonal mean northward atmospheric energy transport (red lines) and zonal mean precipitation (blue) during composite El Niño (solid) and La Niña (dashed) events. The precipitation (precip.) centroid is marked by a star for El Niño and a circle for La Niña. **b**, As in **a** but showing meridional means between 20° S–20° N and eastward instead of northward atmospheric energy transport.

increases on the Equator and decreases near 20° N and 20° S during El Niño, but these changes are relatively small (Fig. 1a). The zonal mean ITCZ, represented by the tropical precipitation centroid (see Methods), shifts southward by about 1° latitude during El Niño. The latitude where zonal mean AET passes through zero, which is called the energy flux equator (EFE) and which has been shown to move meridionally with the ITCZ⁶, shifts southward by even less. These shifts are not expected to fit the 3°-per-petawatt scaling because the net energy input to the equatorial atmosphere (the slope of the AET curve) also changes^{7,8}, from about 15 W m⁻² during La Niña to 20 W m⁻² during El Niño.

These zonal mean shifts are small compared with the east–west shifts that dominate ENSO; although well-known^{26–28}, ENSO's zonal AET changes have not been incorporated into a theory for regional precipitation. We average precipitation and eastward AET between 20° S and 20° N, then calculate the longitude of the precipitation centroid and find locations where the eastward AET is zero. There are four such locations, but only the two in regions of divergent fluxes (where the AET slope is positive) are expected to be associated with precipitating ascent. One lies in the west Pacific (near 150° E) about 500 km east of the global precipitation centroid (Fig. 1b), while the other lies near a secondary rainfall maximum over South America (near 300° E; Supplementary Fig. 1). The precipitation centroid shifts eastward by 22° longitude between La Niña and El Niño composites, and the longitude at which the eastward AET is zero moves eastward by 19°. Thus, precipitation and AET behave as expected for a time-mean tropical overturning circulation, with the precipitation centroid shifting zonally with the location of zero eastward AET.

Divergent energy transports in 2D

Now we generalize these ideas to two dimensions and show qualitative consistency between rainfall and AET for the seasonal cycle and ENSO. Our arguments rest on the idea that the divergent (that is, irrotational) component of time-mean wind, which produces nearly all tropical rainfall²⁹, is closely associated with the divergent component of tropical AET (see Supplementary Information for demonstration of this in a canonical idealized model). Following previous studies^{10,26}, we introduce the ‘energy flux potential’, χ ,

$$\nabla^2 \chi \equiv \nabla \cdot \mathbf{v} h \frac{dp_s}{g} \quad (1)$$

where \mathbf{v} is vector wind, h is moist static energy, g is gravitational acceleration, and with integration from surface pressure p_s to top of the atmosphere (TOA). The gradient of χ is the divergent component of AET, and the Laplacian of χ is, in a seasonal mean, equal to the net energy input to the atmospheric column (energy flows from low to high χ , with χ defined up to an additive constant). There is large zonal and meridional structure in χ in the low-latitude summer hemisphere, indicating that zonal and meridional components of divergent AET, hereafter denoted u_h and v_h , respectively, have comparable magnitudes there (Fig. 2a,b).

Ascending branches of time-mean meridional overturnings are expected to lie near latitudes where both $v_h = 0$ and $\partial_y v_h > 0$ (the EFE), while ascent in time-mean tropical zonal overturnings are expected to lie near longitudes where $u_h = 0$ and $\partial_x u_h > 0$. We call the latter an energy flux prime meridian (EFPM), recognizing that there can be more than one at each latitude. Shifts in the EFE and EFPM (cyan lines in Fig. 2a,b) are thus expected to accompany shifts of time-mean precipitation. This is a generalization to two dimensions of previous constraints on ITCZ latitude^{5–7} and provides information on zonal rainfall variations not available from the EFE alone. Heavy rainfall generally occurs near the EFE, but is enhanced near an EFPM (for example, the Bay of Bengal during boreal summer and the equatorial west Pacific and South America during austral summer). The EFE and EFPM are not exactly collocated with precipitation maxima due to energy advection by rotational flow (see Supplementary Information), transient eddies³⁰, and variations in gross moist stability³¹ (the proportionality constant that relates fluxes of mass and energy¹), yet anomalies in EFE and ITCZ positions have been shown to be highly correlated in regional domains¹⁰.

These ideas can be used to understand changes in divergent AET and rainfall during ENSO. Composites of χ show anomalous energy flux divergence from the east Pacific during El Niño, with strong anomalous zonal AET in the west Pacific (Fig. 2c). The eastward shift in rainfall during El Niño is seen as a zonal dipole in anomalous Pacific rainfall spanning the region of strong anomalous divergent AET. The rainfall maximum shifts in the same direction as the west Pacific EFPM (Fig. 2d), opposite the anomalous divergent AET. Rainfall maxima in the eastern Pacific and over South America also shift with the local EFPM, with weaker rainfall anomalies there consistent with the weaker climatological mean rainfall. Meridional shifts in the South Pacific convergence zone and east Pacific ITCZ also accompany the local EFE shifts, as noted previously¹⁰.

A theory for mid-Holocene precipitation

Six thousand years ago, the July insolation contrast between Earth's poles was enhanced by 30 W m⁻² compared with the present. An ensemble of GCMs collected under the Paleoclimate Modelling Intercomparison Project (PMIP3) simulated a northward shift of the boreal summer ITCZ over Africa and Asia in response to this enhanced insolation gradient (Fig. 3a). But the zonal mean precipitation centroid shifts northward by only 0.2° latitude in the May–September multi-model mean; applying that shift to rainfall at each longitude would produce anomalies not visible using the contour interval of Fig. 3 (for example, the meridional gradient of

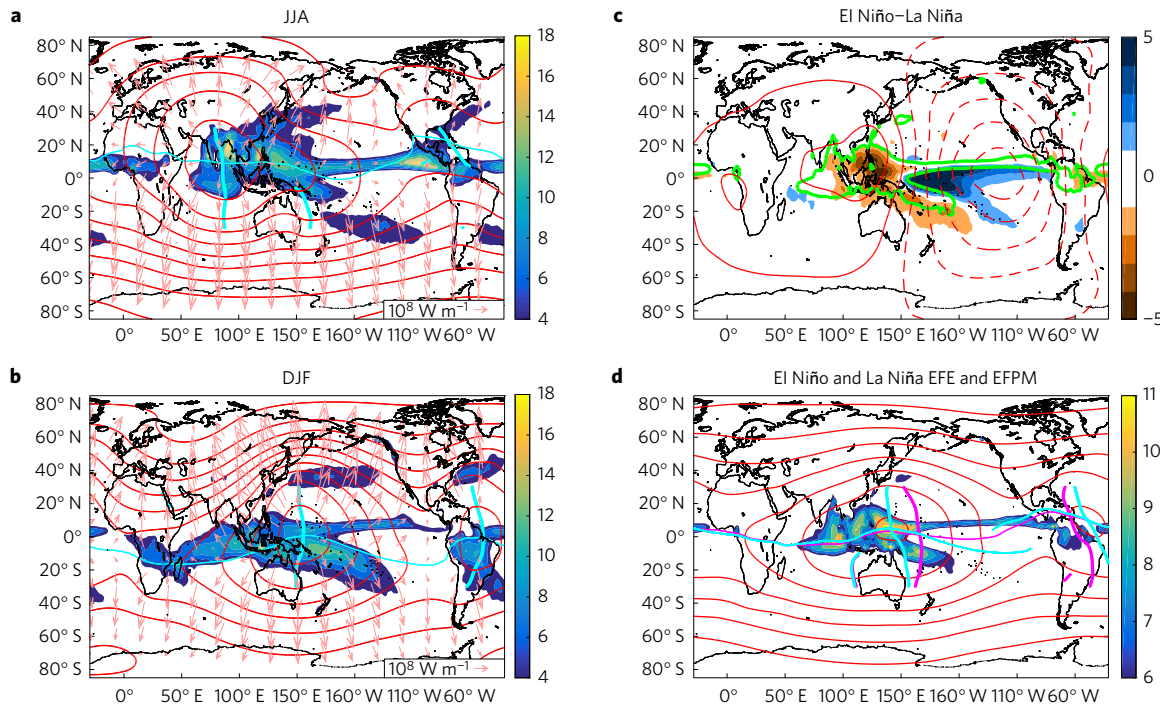


Figure 2 | Two-dimensional views of precipitation and divergent energy transports, visualized using the energy flux potential, χ . **a,b**, Climatologies for June–August (JJA; **a**) and December–February (DJF; **b**) of CMAP precipitation (shading, interval 2 mm d^{-1}), χ (red contours, interval 0.1 PW , with equatorial extrema being minima), the divergent vertically integrated atmospheric energy flux (vectors), and zero lines of the meridional and zonal divergent energy flux (the EFE and EFPM; cyan lines), from ERA-Interim. **c**, Difference between annual mean El Niño and La Niña composites in χ (contours, interval 0.04 PW , negative dashed) and precipitation (shading, interval 1 mm d^{-1}), and the 6 mm d^{-1} total precipitation isoline during La Niña (green contour). **d**, Annual, climatological mean precipitation (shading, interval 1 mm d^{-1}) and χ (contours, interval 0.1 PW), and the EFE and EFPM during El Niño (magenta) and La Niña (cyan).

Sahel precipitation is about 0.8 mm d^{-1} per degree latitude, so a 0.2° shift yields a local change of 0.16 mm d^{-1} .

Anomalous boreal summer AET simulated by PMIP3 models is highly zonally asymmetric, even though the insolation anomaly is zonally symmetric. Relative to pre-industrial climate simulations, the anomalous energy flux potential, χ' , is negative over Northern Hemisphere continents and positive over the Southern Ocean (Fig. 3a, contours), indicating more energy divergence from Northern Hemisphere continents during the mid-Holocene. This response balances the insolation anomaly: seasonally enhanced downward short-wave radiation at the surface can be stored in the ocean mixed layer but enhances upward surface energy fluxes over land, where surface thermal inertia is small, resulting in divergent AET. The region of high pre-industrial boreal summer rainfall (green contour in Fig. 3a) shifts down the gradient in χ' just as it did for ENSO, moving northeastward over Africa and northward over South Asia.

Following ideas presented above, we assume that the precipitation distribution shifts with the local EFE and EFPM. That is, precipitation in two climate states is related by

$$P_2(\phi - \delta_\phi, \lambda - \delta_\lambda) = P_1(\phi, \lambda) \quad (2)$$

where ϕ is latitude, λ is longitude, P is precipitation, and subscripts 1 and 2 denote properties of pre-industrial and mid-Holocene climates, respectively. The meridional and zonal precipitation shifts are

$$\delta_\phi = (\phi_{0,2} - \phi_{0,1}) \mathcal{H}(|\phi - \phi_{0,1}| - \Delta\phi) \quad (3)$$

$$\delta_\lambda = (\lambda_{0,2} - \lambda_{0,1}) \mathcal{H}(|\lambda - \lambda_{0,1}| - \Delta\lambda) \quad (4)$$

where $\phi_{0,i}$ and $\lambda_{0,i}$ are the EFE and EFPM, respectively, in climate state i , and \mathcal{H} is the Heaviside function, introduced to allow a meridional shift only within $\Delta\phi = 20^\circ$ latitude of the EFE and a

zonal shift within $\Delta\lambda = 80^\circ$ longitude of the EFPM. The quantities $\phi_{0,i}$ and $\lambda_{0,i}$ are functions of longitude and latitude, respectively, so a two-dimensional shift can be predicted at each horizontal location. When multiple EFEs exist at a given longitude, (3) is used to obtain δ_ϕ for each EFE and these values are averaged for all EFEs before (2) is computed, with an analogous procedure for multiple EFPMs.

This approach is novel because it predicts shifts in both longitude and latitude, and because it determines those shifts through simple inspection of the altered energy fluxes rather than by approximating those fluxes on the basis of their value at a particular location such as the geographic Equator^{6,7,10} or the unperturbed ITCZ latitude³². Unlike early energy budget theories¹, (2)–(4) do not explicitly include a gross moist stability, but shifting the precipitation distribution with the EFE and EFPM effectively assumes that the gross moist stability distribution undergoes the same two-dimensional shift.

Although shifts in the EFE and EFPM could be obtained from simulated mid-Holocene AET, that approach would be unsatisfying because it requires simulating the anomalous atmospheric state. Instead, we use a theory for the anomalous AET that assumes the fraction $(1 - \alpha_{\text{TOA}})$ of the seasonal insolation anomaly I' not reflected to space is transferred entirely to the atmosphere over land and absorbed entirely by ocean in marine regions, as in previous work^{33–36} (α_{TOA} is TOA albedo). This idealized limit of infinite ocean buffering and vanishing continental thermal inertia yields an anomalous energy source that can be inverted, via the Laplacian, to obtain the distribution of χ' , and thus of u'_h and v'_h , needed to maintain energy balance,

$$\nabla^2 \chi' = (1 - \alpha_{\text{TOA}}) I' L + \frac{(L-1)}{A_O} \int (1 - \alpha_{\text{TOA}}) I' L dA \quad (5)$$

$$u'_h \hat{\mathbf{i}} + v'_h \hat{\mathbf{j}} = \nabla \chi' \quad (6)$$

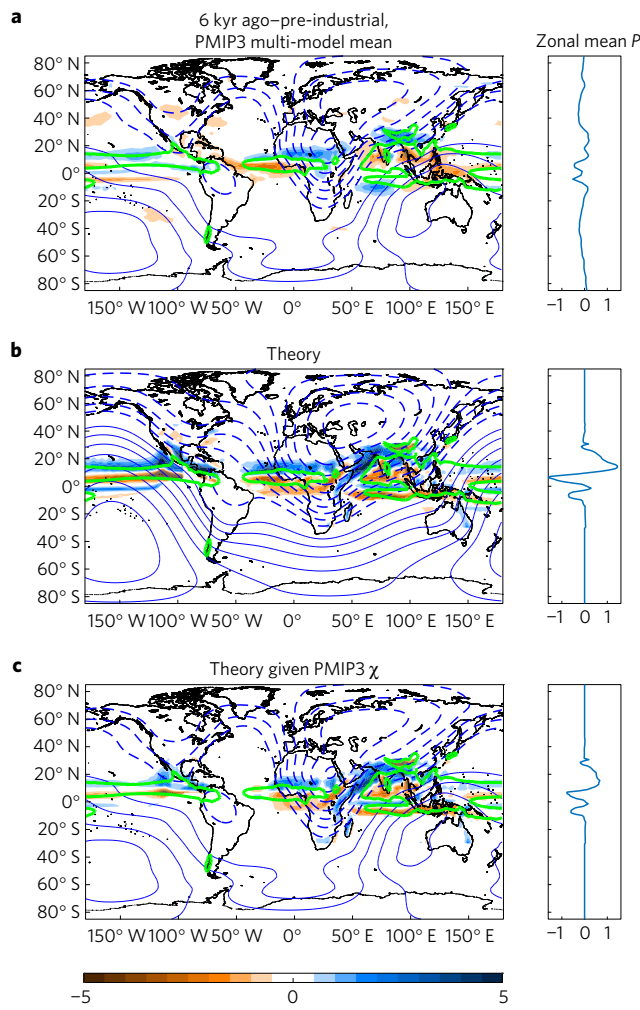


Figure 3 | Climate model simulations and theoretical prediction of boreal summer response to mid-Holocene insolation anomaly. Anomalous χ' (contours) and anomalous precipitation (shading, interval 0.5 mm d^{-1}), 6 kyr ago relative to pre-industrial. **a**, Ensemble mean of PMIP3 models. **b**, Full theoretical prediction (using our theory for anomalous energy flux divergence). **c**, Theoretical prediction using anomalous GCM-simulated energy fluxes. The contour interval in all panels is 0.01 PW with negative contours dashed, and the green contour the 6 mm d^{-1} precipitation isoline from the pre-industrial multi-model mean. All quantities are May–September climatological means. The panels on the right show zonal means (over all longitudes) of the precipitation anomaly in mm d^{-1} .

where L is the local land fraction, A_O is the global ocean surface area, and we integrate globally. To avoid using information from the altered climate state (the mid-Holocene) as input to the theory, we use model-simulated pre-industrial albedo for α_{TOA} . Despite these idealized assumptions, the resulting distribution of χ' (Fig. 3b, contours) decently matches that simulated by GCMs over Africa and Eurasia (Fig. 3a). Larger deviations occur over ocean, which is not surprising since ocean is not a uniform sink for anomalous radiation. The fit is not as good for individual models, although all show qualitatively similar spatial structure (Supplementary Fig. 6). Overall, it is remarkable that continental maxima of χ' are predicted so well given only modern albedo and orbital parameters.

When (6) is used to turn this theoretical χ' into an energy flux anomaly and (2)–(4) are then used to find the rainfall shift, we obtain a theoretical prediction of mid-Holocene rainfall. This consists of a northward shift of rainfall maxima in most longitudes, a westward shift in the Indian Ocean, and an eastward shift over

Central America (Fig. 3b). Although there is anomalous westward energy flux over much of Africa, the theory predicts no eastward rainfall shift there because no EFPM exists over Africa (for example, Fig. 2a). The theory predicts too large a shift in the east Pacific and Central America, consistent with its poorer skill in representing oceanic χ' . Indeed, when the GCM-simulated χ' is used in the theory instead of (5)–(6), the difference between the theory and GCMs is reduced over the east Pacific and Central America (Fig. 3c). The theory predicts strongly enhanced western Indian Ocean rainfall regardless of whether we use (5)–(6) or the simulated χ' , while the GCMs simulate weak drying there.

Our theory for the mid-Holocene rainfall anomaly matches that simulated by the GCMs remarkably well over North Africa (Fig. 4a), indicating that GCM-simulated rainfall changes there can be understood as the ITCZ shift needed to maintain energy balance given the two-dimensional distribution of the absorbed short-wave anomaly. The fit improves mildly when the model-simulated anomalous AET is used in the theory instead of (5)–(6), suggesting that radiative feedbacks make a small contribution to the perturbed AET. Thus, the simulated moist atmospheric dynamics respond to the orbital forcing as expected given our understanding of the atmospheric energy budget; if this response is too weak compared with proxies¹⁵, some other mechanism is probably involved. Furthermore, using observed distributions of present-day albedos, energy fluxes, and precipitation as input to our theory produces similar results (Fig. 4b), showing that model bias does not compromise the theoretical predictions.

Pollen-based reconstructions suggest that annual rainfall was $350 \pm 150 \text{ mm}$ higher 20°N – 30°N over Africa in the mid-Holocene than today¹². If this all fell during May–September, an average increase of 1.2 to 3.6 mm d^{-1} is required during those months. The GCM multi-model mean is below this range, as is the theoretical prediction based on the insolation change (Fig. 4).

Previous GCM simulations suggest that vegetation or soil colour feedbacks were required to reach this precipitation range^{17,19,21}, which motivates using our theory to predict the response to reduced Saharan surface albedo. We reduce North African surface albedo larger than 0.15 to 0.15 (see Methods), and then estimate the anomalous divergent AET needed to maintain energy balance. We estimate this AET by multiplying pre-industrial insolation, I , by the surface albedo change, $\Delta\alpha_s$, and by the sensitivity of α_{TOA} to surface albedo (this sensitivity, linearized about the modern Saharan atmospheric state, is 0.73 ; see Methods),

$$\nabla^2 \chi' \simeq -I \frac{\partial \alpha_{\text{TOA}}}{\partial \alpha_s} \Delta\alpha_s \quad (7)$$

We sum the right-hand sides of (7) and (5) to obtain a linearization of the AET divergence produced by the combined albedo and insolation change, then invert this to obtain χ' and use (6) and (2)–(4) to obtain the precipitation shift. When this precipitation anomaly is averaged over African longitudes, summer rain rates of 1 – 3 mm d^{-1} are found over the southern Sahara, within the proxy range in that region (Fig. 4). The predicted precipitation increase over the Sahel, near 15° N , is about four times the direct response to the insolation anomaly. The direct energy source from the insolation forcing (that is, the right-hand side of (5)) is roughly 10 W m^{-2} over most tropical and subtropical Northern Hemisphere land, while the energy source from the albedo change (the right-hand side of (7)) is around 70 W m^{-2} but is confined to the Saharan region; the theory appropriately weights the area, magnitude, and location of these forcings to gauge the expected response.

Since Eurasian afforestation was argued to have enhanced mid-Holocene Saharan rainfall²², we also use the theory to calculate the response to a reduction of land surface albedo to 85% of its pre-industrial value everywhere north of 30° N outside of North Africa and Greenland (including North America). Our sensitivity factor

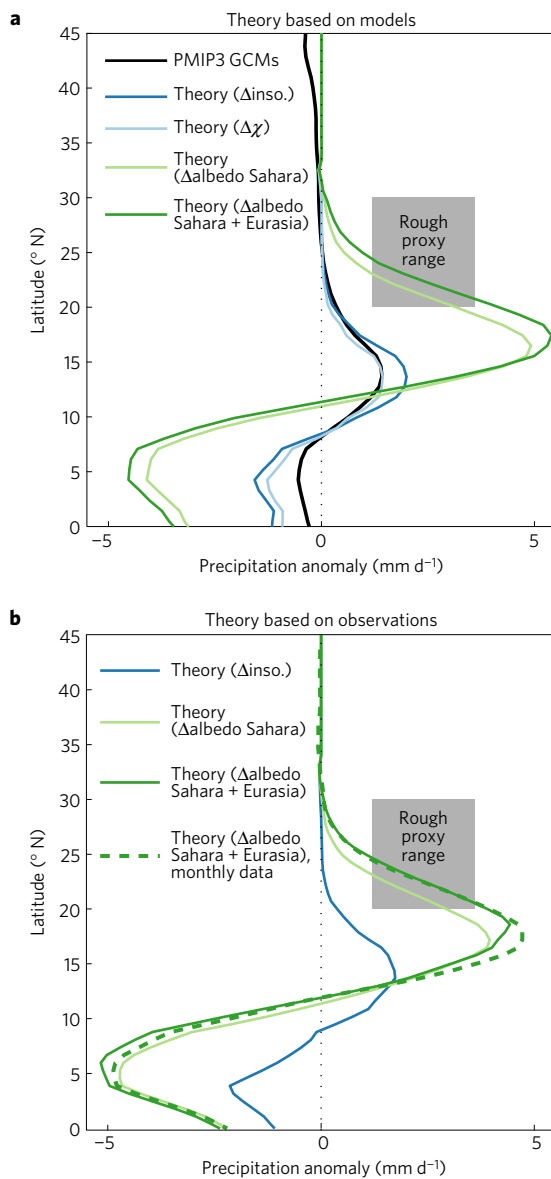


Figure 4 | Response of African summer rainfall to mid-Holocene insolation and albedo changes. **a**, Limited zonal means over Africa (20°W – 40°E) of the precipitation difference between mid-Holocene and pre-industrial for: PMIP3 ensemble mean (black); theory using mid-Holocene insolation ($\Delta_{\text{inso.}}$) change and PMIP3 pre-industrial climate as input (dark blue); theory using PMIP3-simulated mid-Holocene energy transport anomaly (light blue); theory assuming a maximum Saharan surface albedo of 0.15 (light green); and theory assuming the Saharan albedo change plus Northern Hemisphere land surface albedo reduced to 85% of pre-industrial values (dark green). All are May–September climatological means. The grey rectangle marks the range of mid-Holocene boreal summer Saharan precipitation increase from pollen-based reconstructions. **b**, As in **a** but using observed precipitation, energy fluxes and albedo as input to the theory. The dashed line uses monthly mean rather than seasonal mean data as input.

$\partial\alpha_{\text{TOA}}/\partial\alpha_s$ is probably too large for those non-desert regions, but this forcing is meant to be idealized and could be taken to represent changes in both vegetation and cloudiness. As in a previous GCM²², this remote albedo change produces a modest enhancement of the response to the Saharan albedo reduction (Fig. 4). Even this response lies well below the proxy range over the Sahara north of 25°N , but proxies are sparse there (for example, only two grid points of proxy

data contribute between 25° and 30°N (ref. 14)) and precipitation outside of May–September may be important in that region²¹. Cloud feedbacks may modify the energy budget³⁷, but the short-wave and long-wave effects of tropical clouds on the column-integrated energy budget are expected to roughly cancel³⁸; they do not produce large disagreement between our theory and the GCM ensemble mean. More important might be the reduction in Saharan surface temperature expected to occur in response to local moistening, which would reduce long-wave cooling to space and enhance the precipitation shift.

Concluding remarks

Our theory for orbitally forced precipitation change requires only the insolation anomaly and the unperturbed climate state (that is, pre-industrial precipitation, AET, and TOA albedo), and does not require running a climate model to simulate the altered AET. It shows that, in boreal summer, the mid-Holocene is characterized by enhanced energy transport away from Northern Hemisphere continents and a northward or inland shift in rainfall maxima. The magnitude and direction of the anomalous divergent AET and of the regional rainfall shift are set by the seasonal insolation anomaly rectified by the land-sea distribution. In our theory, rainfall necessary to sustain a vegetated Sahara requires a large positive feedback on the insolation anomaly; given the small response to Eurasian TOA albedo change, Saharan surface albedo change seems a good candidate, consistent with suggestions based on previous GCM simulations^{17,19,21}.

Our theory could be applied to other climate perturbations, such as Heinrich events³⁹, regional aerosol emissions⁴⁰, or the transient response to volcanic eruptions⁴¹. Caveats merit exploration, such as the effect of cloud and surface temperature feedbacks on the anomalous energy source. Although this is a theory for rainfall shifts, not rainfall changes in general, it provides a step toward a quantitative, predictive theory for regional changes produced by arbitrary energy sources.

Methods

Methods, including statements of data availability and any associated accession codes and references, are available in the online version of this paper.

Received 1 June 2016; accepted 7 October 2016;
published online 21 November 2016

References

1. Neelin, J. D. & Held, I. M. Modeling tropical convergence based on the moist static energy budget. *Mon. Weath. Rev.* **115**, 3–12 (1987).
2. Chiang, J. C. H. & Bitz, C. M. Influence of high latitude ice cover on the marine Intertropical Convergence Zone. *Clim. Dynam.* **25**, 477–496 (2005).
3. Broccoli, A. J., Dahl, K. A. & Stouffer, R. J. Response of the ITCZ to Northern Hemisphere cooling. *Geophys. Res. Lett.* **33**, L01702 (2006).
4. Chiang, J. C. & Friedman, A. R. Extratropical cooling, interhemispheric thermal gradients, and tropical climate change. *Annu. Rev. Earth Planet. Sci.* **40**, 383–412 (2012).
5. Kang, S. M., Held, I. M., Frierson, D. M. W. & Zhao, M. The response of the ITCZ to extratropical thermal forcing: idealized slab-ocean experiments with a GCM. *J. Clim.* **21**, 3521–3532 (2008).
6. Donohoe, A., Marshall, J., Ferreira, D. & McGee, D. The relationship between ITCZ location and cross-equatorial atmospheric heat transport: from the seasonal cycle to the last glacial maximum. *J. Clim.* **26**, 3597–3618 (2013).
7. Bischoff, T. & Schneider, T. Energetic constraints on the position of the intertropical convergence zone. *J. Clim.* **27**, 4937–4951 (2014).
8. Schneider, T., Bischoff, T. & Haug, G. H. Migrations and dynamics of the intertropical convergence zone. *Nature* **513**, 45–53 (2014).
9. McGee, D., Donohoe, A., Marshall, J. & Ferreira, D. Changes in ITCZ location and cross-equatorial heat transport at the Last Glacial Maximum, Heinrich Stadial 1, and the mid-Holocene. *Earth Planet. Sci. Lett.* **390**, 69–79 (2014).
10. Adam, O., Bischoff, T. & Schneider, T. Seasonal and interannual variations of the energy flux equator and ITCZ. Part II: Zonally varying shifts of the ITCZ. *J. Clim.* **29**, 7281–7293 (2016).

11. Jolly, D. *et al.* Biome reconstruction from pollen and plant macrofossil data for Africa and the Arabian peninsula at 0 and 6000 years. *J. Biogeogr.* **25**, 1007–1027 (1998).
12. Bartlein, P. J. *et al.* Pollen-based continental climate reconstructions at 6 and 21 ka: a global synthesis. *Clim. Dynam.* **37**, 775–802 (2011).
13. Perez-Sanz, A., Li, G., Gonzalez-Sameriz, P. & Harrison, S. P. Evaluation of modern and mid-Holocene seasonal precipitation of the Mediterranean and northern Africa in the CMIP5 simulations. *Clim. Past* **10**, 551–568 (2014).
14. Harrison, S. P. *et al.* Evaluation of CMIP5 palaeo-simulations to improve climate projections. *Nat. Clim. Change* **5**, 735–743 (2015).
15. Harrison, S. P. *et al.* Climate model benchmarking with glacial and mid-Holocene climates. *Clim. Dynam.* **43**, 671–688 (2014).
16. Harrison, S. P. *et al.* Intercomparison of simulated global vegetation distributions in response to 6 kyr BP orbital forcing. *J. Clim.* **11**, 2721–2742 (1998).
17. Joussaume, S. *et al.* Monsoon changes for 6000 years ago: results of 18 simulations from the Paleoclimate Modeling Intercomparison Project (PMIP). *Geophys. Res. Lett.* **26**, 859–862 (1999).
18. Bonfils, C., De Noblet-Ducoudré, N. D., Braconnot, P. & Joussaume, S. Hot desert albedo and climate change: mid-Holocene monsoon in North Africa. *J. Clim.* **14**, 3724–3737 (2001).
19. Lewis, S., Bonan, G. B. & Bonfils, C. Soil feedback drives the mid-Holocene North African monsoon northward in fully coupled CCSM2 simulations with a dynamic vegetation model. *Clim. Dynam.* **23**, 791–802 (2004).
20. Su, H. & Neelin, J. D. Dynamical mechanisms for African monsoon changes during the mid-Holocene. *J. Geophys. Res.* **110**, 19105 (2005).
21. Skinner, C. B. & Poulsen, C. J. The role of fall season tropical plumes in enhancing Saharan rainfall during the African Humid Period. *Geophys. Res. Lett.* **43**, 349–358 (2016).
22. Swann, A. L. S., Fung, I. Y., Liu, Y. & Chiang, J. C. H. Remote vegetation feedbacks and the mid-Holocene green Sahara. *J. Clim.* **27**, 4857–4870 (2014).
23. Held, I. M. & Soden, B. J. Robust responses of the hydrological cycle to global warming. *J. Clim.* **19**, 5686–5699 (2006).
24. Boos, W. R. Thermodynamic scaling of the hydrological cycle of the last glacial maximum. *J. Clim.* **25**, 992–1006 (2012).
25. Clement, A. C., Hall, A. & Broccoli, A. J. The importance of precessional signals in the tropical climate. *Clim. Dynam.* **22**, 327–341 (2004).
26. Trenberth, K. E., Stepaniak, D. P. & Caron, J. M. Interannual variations in the atmospheric heat budget. *J. Geophys. Res.* **107**, 4066 (2002).
27. Mayer, M., Trenberth, K. E., Haimberger, L. & Fasullo, J. T. The response of tropical atmospheric energy budgets to ENSO. *J. Clim.* **26**, 4710–4724 (2013).
28. Mayer, M., Haimberger, L. & Balmaseda, M. A. On the energy exchange between tropical ocean basins related to ENSO. *J. Clim.* **27**, 6393–6403 (2014).
29. Seager, R. & Henderson, N. Diagnostic computation of moisture budgets in the ERA-interim reanalysis with reference to analysis of CMIP-archived atmospheric model data. *J. Clim.* **26**, 7876–7901 (2013).
30. Peters, M. E., Kuang, Z. & Walker, C. C. Analysis of atmospheric energy transport in ERA-40 and implications for simple models of the mean tropical circulation. *J. Clim.* **21**, 5229–5241 (2008).
31. Back, L. E. & Bretherton, C. S. Geographic variability in the export of moist static energy and vertical motion profiles in the tropical Pacific. *Geophys. Res. Lett.* **33**, 1–5 (2006).
32. Shekhar, R. & Boos, W. R. Improving energy-based estimates of monsoon location in the presence of proximal deserts. *J. Clim.* **29**, 4741–4761 (2016).
33. Braconnot, P., Marti, O., Joussaume, S. & Leclainche, Y. Ocean feedback in response to 6 kyr BP Insolation. *J. Clim.* **13**, 1537–1553 (2000).
34. Chou, C. & Neelin, J. D. Mechanisms limiting the northward extent of the northern summer monsoons over North America, Asia, and Africa. *J. Clim.* **16**, 406–425 (2003).
35. Hsu, Y. H., Chou, C. & Wei, K. Y. Land-ocean asymmetry of tropical precipitation changes in the mid-Holocene. *J. Clim.* **23**, 4133–4151 (2010).
36. Merlis, T. M., Schneider, T., Bordoni, S. & Eisenman, I. Hadley circulation response to orbital precession. Part II: Subtropical continent. *J. Clim.* **26**, 754–771 (2013).
37. Hwang, Y. T. & Frierson, D. M. W. Increasing atmospheric poleward energy transport with global warming. *Geophys. Res. Lett.* **37**, L24807 (2010).
38. Kiehl, J. T. On the observed near cancellation between longwave and shortwave cloud forcing in tropical regions. *J. Clim.* **7**, 559–565 (1994).
39. Behling, H., Arz, H. W., Pätzold, J. & Wefer, G. Late Quaternary vegetational and climate dynamics in northeastern Brazil, inferences from marine core GeoB 3104-1. *Quat. Sci. Rev.* **19**, 981–994 (2000).
40. Ramanathan, V. *et al.* Atmospheric brown clouds: impacts on South Asian climate and hydrological cycle. *Proc. Natl Acad. Sci. USA* **102**, 5326–5333 (2005).
41. Robock, A., Mu, M., Vinnikov, K. & Robinson, D. Land surface conditions over Eurasia and Indian summer monsoon rainfall. *J. Geophys. Res.* **108**, 4131 (2003).

Acknowledgements

W.R.B. was supported by National Science Foundation (NSF) grants AGS-1253222 and AGS-1515960, and by Office of Naval Research grant N00014-15-1-2531. R.L.K. was supported by NSF grant AGS-1064013. W.R.B. thanks D. McGee and M. Biasutti for helpful discussions, and A. Voigt and A. Donohoe for comments that improved the manuscript.

Author contributions

W.R.B. conceived the study, devised and applied the theory to the PMIP models and observational data, and integrated and analysed the idealized model described in the Supplementary Information. R.L.K. analysed the PMIP data, and both authors contributed to writing the manuscript and interpreting results.

Additional information

Supplementary information is available in the online version of the paper. Reprints and permissions information is available online at www.nature.com/reprints. Correspondence and requests for materials should be addressed to W.R.B.

Competing financial interests

The authors declare no competing financial interests.

Methods

Data and analysis methods. Atmospheric energy fluxes were derived from ERA-Interim, the most recent reanalysis of the European Centre for Medium-Range Weather Forecasts (ECMWF)⁴². In particular, we used monthly mean vertically integrated atmospheric moist energy fluxes for 1979–2013 provided by the National Center for Atmospheric Research (<http://climatedataguide.ucar.edu/climate-data/era-interim-derived-components>). These energy fluxes were calculated using a method that eliminates the residual from the vertically integrated mass budget in each 6-hourly estimate of the atmospheric state by subtracting a barotropic wind from the horizontal wind at each level^{43,44}; the corrected winds were then used to calculate vertically integrated, monthly mean atmospheric energy fluxes. Here we averaged those monthly mean fluxes of total energy (including latent heat and kinetic energy) over the 35 years of the data set. All boreal summer means were taken from May–September, which coincides with the period during which the mid-Holocene insolation anomaly is positive (Supplementary Fig. 4).

Precipitation data were obtained from the Climate Prediction Center (CPC) Merged Analysis of Precipitation (CMAP) provided by NOAA/OAR/ESRL PSD, Boulder, Colorado, USA, from their web site at <http://www.esrl.noaa.gov/psd/>. This data set provides monthly mean estimates of precipitation rates based on satellite data⁴⁵. The CMAP estimates are available from 1979 through the present, but we used only 1979–2013 for consistency with the ERA-Interim energy fluxes.

Surface and TOA broadband short-wave albedos, defined as the fraction of all incident short-wave radiation that is reflected, were obtained using estimated short-wave fluxes from the Clouds and the Earth's Radiant Energy System (CERES) product. In particular, we used energy balanced and filled TOA and surface all-sky fluxes for years 2001–2015, obtained from the NASA CERES website (<http://ceres.larc.nasa.gov>). These observed surface and TOA albedos were used only in Fig. 4b.

ENSO events were classified by the Oceanic Niño Index (ONI), an indicator used by the National Oceanic and Atmospheric Administration (NOAA) to monitor ENSO. The ONI is the 3-month running mean of SST anomalies in the Niño 3.4 region (5° S– 5° N, 120° – 170° W), based on the Extended Reconstructed SST⁴⁶, version 4. Anomalies were computed relative to centred 30-year means updated every 5 years. Here we classify a year as El Niño when the ONI exceeds $+0.5$ K (or -0.5 K for La Niña) for at least 8 out of 12 months of the year, with a year running from July through the following June for consistency with the typical spring/summer onset of ENSO events. The El Niño and La Niña states shown in Figs 1 and 2 are simple composites obtained by averaging over all events defined in this manner. Supplementary Fig. 2 shows El Niño and La Niña states constructed using an alternate regression methodology; the zonal shift in the EFPM is smaller than the zonal shift in the precipitation centroid when ENSO states are constructed in that manner.

We analysed four members of the PMIP3 ensemble in this analysis (PMIP3 is part of the Fifth Coupled Model Intercomparison Project, CMIP5); we included those members for which all necessary TOA and surface fluxes of radiation and enthalpy were available for both the mid-Holocene and pre-industrial era control experiments. Model names and brief characteristics are listed in Supplementary Table 2. The simulations were performed with models having coupled ocean and atmosphere components or ocean, atmosphere and carbon cycle components. Details of the PMIP3 integrations are provided in previous literature⁴⁷. In summary, the mid-Holocene simulations contain 280 ppmv CO₂, as in the pre-industrial era control, but differ from it in that CH₄ is slightly lower (650 ppbv at mid-Holocene; 760 ppbv at pre-industrial era) and orbital parameters for 6 kyr ago were prescribed.

The precipitation centroid is defined as the geographic centre of mass of the precipitation distribution. The centroid of zonal mean precipitation is calculated using only precipitation between 20° N and 20° S, so that half of the area-integrated precipitation within that domain falls south of the centroid and half falls to the north. When the longitudinal centroid of the meridionally averaged (20° N– 20° S) precipitation is computed, the centre of mass is calculated using circular statistics⁴⁸ in a global domain; restricting the domain to the Indo-Pacific region made little difference in the results. Precipitation was interpolated to a 0.01° grid before calculating the centroid; the same was done for the meridional energy fluxes when calculating the location of zero lines of the zonal and meridional energy fluxes.

Our theoretical estimates were calculated using boreal summer mean inputs, with boreal summer defined as May–September. Small changes in these theoretical estimates occur when they are calculated using climatological monthly mean inputs and then seasonally averaged (for example, dashed and solid dark green lines in Fig. 4b use monthly and seasonal mean data, respectively, to estimate the response to Saharan plus Eurasian albedo change).

We also tested the sensitivity of applying our theory to the distribution of precipitation P minus surface evapotranspiration E , which is the net surface water input and is thus more relevant to proxies such as lake levels. Both the model and theoretical responses of $P-E$ to mid-Holocene insolation are muted, compared with the P response, over northern Africa and other Northern Hemisphere land regions. But this is expected since $P-E$ is generally smaller than P , and the general

patterns and model–theory agreement are similar (Supplementary Fig. 5). One exception is that there are some intense coastal anomalies of $P-E$ in the theoretical response that do not occur in the climate models; these are caused by the theory shifting the strong gradient of E that exists between ocean and dry land regions.

Sensitivity of AET divergence to surface albedo. Over land, where surface thermal inertia is small, a time-mean anomaly in divergent AET must be balanced by changes in short-wave (SW) and long-wave (LW) fluxes at TOA,

$$\nabla^2 \chi' = \Delta SW + \Delta LW \quad (8)$$

The TOA radiative flux changes can be decomposed into components associated with changes in insolation, surface albedo, cloud fraction c , aerosol optical depth τ , and surface temperature T_s ,

$$\Delta SW = (1 - \alpha_{TOA}) \Delta I - I \left. \frac{\partial \alpha_{TOA}}{\partial \alpha_S} \right|_{c,\tau} \Delta \alpha_S - I \left. \frac{\partial \alpha_{TOA}}{\partial c} \right|_{\alpha_S,\tau} \Delta c - I \left. \frac{\partial \alpha_{TOA}}{\partial \tau} \right|_{\alpha_S,c} \Delta \tau \quad (9)$$

$$\Delta LW = \left. \frac{\partial LW}{\partial T_S} \right|_{c,\tau} \Delta T_S + \left. \frac{\partial LW}{\partial c} \right|_{T_S,\tau} \Delta c + \left. \frac{\partial LW}{\partial \tau} \right|_{T_S,c} \Delta \tau \quad (10)$$

where we have assumed the short-wave budget is not directly sensitive to T_S and the long-wave budget is not directly sensitive to α_S . In the main text, we assumed that the changes in long-wave and short-wave cloud radiative forcings approximately cancel³⁸. This leaves terms involving changes in insolation, surface albedo, surface temperature, and aerosol optical depth, each of which contains sensitivities that can be linearized about the modern state of the Saharan atmosphere.

The modern atmosphere contains few clouds over the Sahara, so we used semi-empirical relations to quantify the sensitivity of TOA albedo to surface albedo ($\partial \alpha_{TOA} / \partial \alpha_S$) under clear-sky conditions. A single equation was previously derived to obtain α_S from α_{TOA} as a function of solar zenith angle and precipitable water⁴⁹; for low zenith angles and values of precipitable water typical of those found over the Sahara in modern climate (about 20 mm), this equation can be inverted to obtain $\partial \alpha_{TOA} / \partial \alpha_S = 0.73$. This value is the same as that presented in an earlier linear estimate that was independent of zenith angle and humidity⁵⁰ and is chosen for our analysis.

To further validate this choice of $\partial \alpha_{TOA} / \partial \alpha_S$, we used a Gamma-weighted two-stream radiative transfer scheme (the Ed4 LaRC Fu–Liou model)⁵¹ with an idealized atmospheric profile representative of conditions over a desert. We prescribed precipitable water of 20 mm, a diurnal-mean lapse rate of 8.5 K km^{-1} , a skin temperature of 300 K, and zero clouds and aerosol. For a change in surface albedo from 0.2 to 0.3, we obtained a linearized estimate of $\partial \alpha_{TOA} / \partial \alpha_S = 0.70$ when $\tau = 0$, with only a weak dependence on solar zenith angle for most zenith angles. Then we used an idealized dust aerosol with particle size of $1 \mu\text{m}$, scale height of 4 km, and optical depth $\tau = 0.4$ to represent dusty conditions over the Sahara, and found that this sensitivity decreased to 0.5–0.6 depending on solar zenith angle. However, the change in τ from 0.0 to 0.4 alone produced a change in TOA albedo of 0.02–0.06 depending on solar zenith angle. Thus, our choice of $\partial \alpha_{TOA} / \partial \alpha_S = 0.73$ is too large if dust aerosol is present over the Sahara, but the effect of this error on ΔSW will be compensated by the reduction in τ expected to accompany a greening of the Sahara. If the changes in τ are expressed as a function of changes in α_S , then the ‘effective’ sensitivity of TOA albedo to surface albedo (that includes an accompanying change in aerosol optical depth) will typically be larger than 0.7 and can even exceed unity. As mentioned in the main text, the reduction in land surface albedo will also probably be accompanied by cooling and moistening of the surface that would reduce long-wave cooling to space (first term on right-hand side of (10)), providing an additional positive feedback on the albedo forcing. Thus, our choice of the clear-sky value of $\partial \alpha_{TOA} / \partial \alpha_S = 0.73$ does neglect the influence of dust aerosol, but changes in that aerosol and in land surface temperature should provide positive feedbacks that compensate for the effects of any overestimate in $\partial \alpha_{TOA} / \partial \alpha_S$. Whether changes in clouds would provide a non-negligible net change in net TOA radiation over the Sahara merits further exploration.

Data availability. The data that support the findings of the study can be accessed as follows: the monthly mean vertically integrated atmospheric moist energy fluxes for 1979–2013 can be obtained from <http://climatedataguide.ucar.edu/climate-data/era-interim-derived-components>.

Precipitation data can be obtained from the Climate Prediction Center (CPC) Merged Analysis of Precipitation (CMAP) at <http://www.esrl.noaa.gov/psd/>.

The energy balanced and filled TOA and surface all-sky fluxes for years 2001–2015 can be obtained from <http://ceres.larc.nasa.gov>.

Output from the Paleoclimate Modelling Intercomparison Project 3 (PMIP3) simulations are available through the Coupled Model Intercomparison Project 5 (CMIP5) data portal at <http://cmip-pcmdi.llnl.gov/cmip5>.

The Oceanic Niño Index (ONI) data were obtained from <https://catalog.data.gov/dataset/climate-prediction-center-cpc-oceanic-nino-index>.

References

42. Dee, D. P. *et al.* The ERA-Interim reanalysis: configuration and performance of the data assimilation system. *Q. J. R. Meteorol. Soc.* **137**, 553–597 (2011).
43. Trenberth, K. E. Using atmospheric budgets as a constraint on surface fluxes. *J. Clim.* **10**, 2796–2809 (1997).
44. Trenberth, K. E., Caron, J. M. & Stepaniak, D. P. The atmospheric energy budget and implications for surface fluxes and ocean heat transports. *Clim. Dynam.* **17**, 259–276 (2001).
45. Xie, P. & Arkin, P. A. Analyses of global monthly precipitation using gauge observations, satellite estimates, and numerical model predictions. *J. Clim.* **9**, 840–858 (1996).
46. Huang, B. *et al.* Extended reconstructed sea surface temperature version 4 (ERSSTv4). Part I: upgrades and intercomparisons. *J. Clim.* **28**, 911–930 (2015).
47. Braconnot, P. *et al.* Evaluation of climate models using palaeoclimatic data. *Nat. Clim. Change* **2**, 417–424 (2012).
48. Jammalamadaka, S. R. & SenGupta, A. *Topics in Circular Statistics* (World Scientific Publishing Co. Pte. Ltd, 2001).
49. Li, Z. & Garand, L. Estimation of surface albedo from space: a parameterization for global application. *J. Geophys. Res.* **99**, 8335–8350 (1994).
50. Chen, T. S. & Ohring, G. On the relationship between clear-sky planetary and surface albedos. *J. Atmos. Sci.* **41**, 156–158 (1984).
51. Fu, Q., Liou, K. N., Cribb, M. C., Charlock, T. P. & Grossman, A. Multiple scattering parameterization in thermal infrared radiative transfer. *J. Atmos. Sci.* **54**, 2799–2812 (1997).

In the format provided by the authors and unedited.

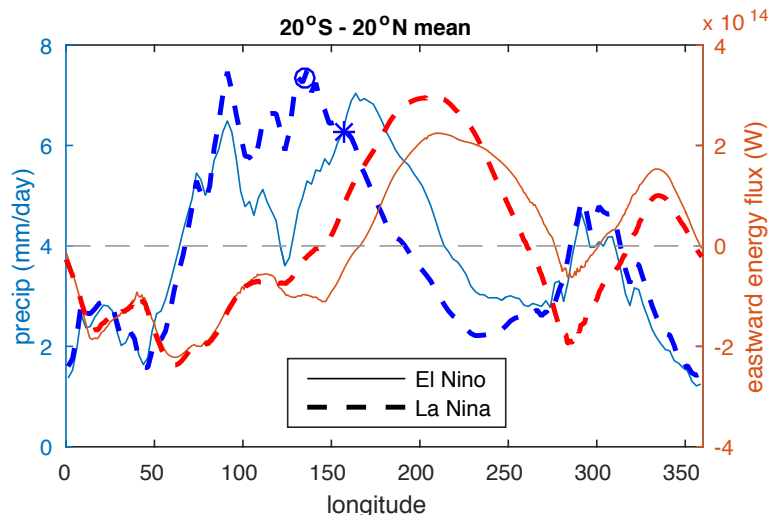
Regional energy budget control of the intertropical convergence zone and application to mid-Holocene rainfall

WILLIAM R. BOOS*

*Department of Geology and Geophysics
Yale University, New Haven, Connecticut, 06511, USA*

ROBERT L. KORTY

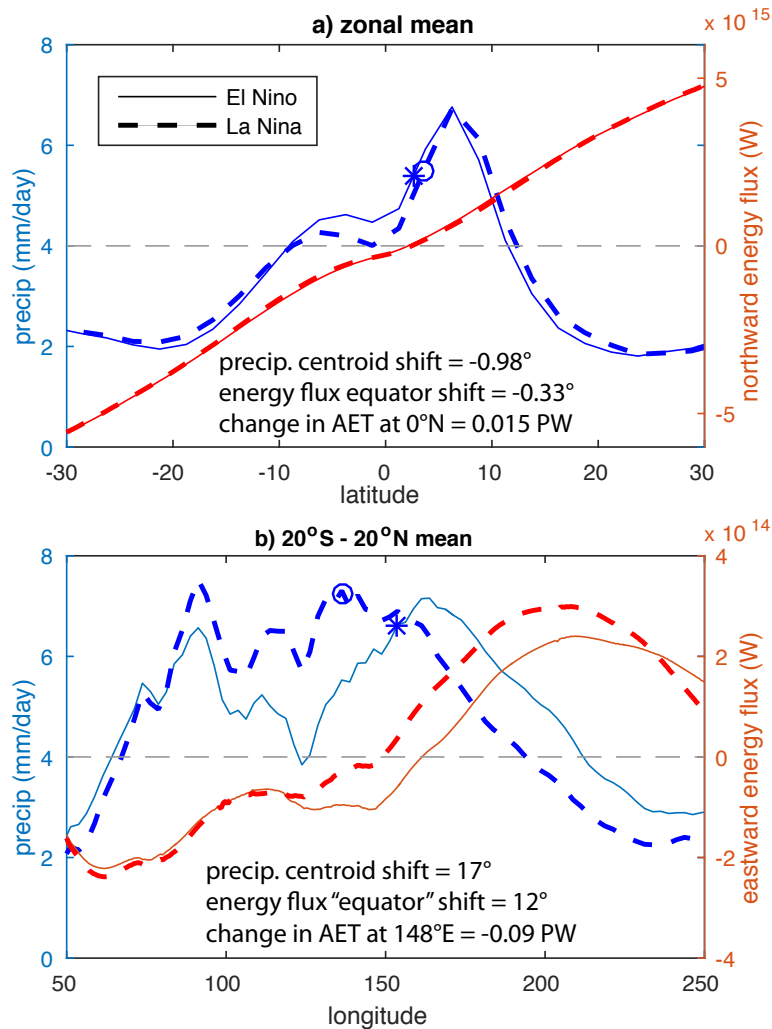
*Department of Atmospheric Sciences
Texas A&M University, College Station, Texas, 77843, USA*



SUPPLEMENTARY FIGURE 1. Same as Fig. 1b of main text, but for the entire tropics rather than a limited range of longitudes.

E-mail addresses: billboos@alum.mit.edu.

SUPP. INFORMATION: REGIONAL ENERGY BUDGET CONTROL OF THE ITCZ



SUPPLEMENTARY FIGURE 2. Same as Fig. 1 of main text, but with El Niño and La Niña states constructed using linear regression (rather than composite averaging). Precipitation and AET are regressed on the NOAA ONI, then these regression coefficients are multiplied by one standard deviation of the ONI and added to the long-term climatological mean of each quantity to produce the El Niño state; the regression coefficients are multiplied by -1 in this procedure to produce the La Niña state.

SUPP. INFORMATION: REGIONAL ENERGY BUDGET CONTROL OF THE ITCZ

1. ASSOCIATION OF DIVERGENT ENERGY FLUXES WITH RAINFALL

The association between divergent winds and divergent AET is ensured for the zonal mean because nearly all zonal mean tropical AET is produced by the zonal mean meridional circulation, which by definition is purely divergent (i.e. irrotational). But at a particular longitude, the divergent AET could be nonzero even when the wind is exactly non-divergent, and in the tropics it is the time mean divergent wind that produces nearly all time mean rainfall¹. In other words, in a zonally asymmetric climate, might rotational tropical winds balance a regional energy source through horizontal energy advection? Here we show that in one of the classic, idealized models for the zonally asymmetric circulation of Earth's tropical and subtropical troposphere, the divergent component of time mean winds produces most (i.e. more than half) of the vertically integrated energy flux divergence. This association between rainfall and the two-dimensional distribution of energy flux divergence in an idealized model motivates and helps justify the analyses conducted in the main text.

1.1. Model details and methods. We construct a fully nonlinear numerical version of the “Gill model”, a canonical theoretical model for the atmospheric response to a zonally confined heat source². When this heat source is positioned off the equator, previous solutions to the Gill model include many of the large-scale features of observed monsoons, with ascent near the heat source, subsidence to the west, and a zonal mean cross-equatorial Hadley circulation³. Here we construct a numerical version of the Gill model using version 5.1 of the Community Atmosphere Model (CAM5.1) produced by the National Center for Atmospheric Research. The original Gill model^{2;3} lacked explicit moisture and imposed a diabatic heat source meant to represent a zonally confined precipitation maximum; since we wish to study energy transports in a moist, precipitating atmosphere we configure our model with a fully interactive hydrological cycle and an entirely oceanic surface (i.e. we run it in “aquaplanet” mode). A zonally confined, off-equatorial precipitation maximum is created by imposing a Gaussian sea surface temperature (SST) maximum centered at 25°N, 90°E — in roughly the location of the South Asian monsoon — on an otherwise globally uniform background SST of 300 K. The Gaussian SST anomaly has peak amplitude of 4 K and horizontal length scales (i.e. standard deviations) of 15° in longitude and 7.5° in latitude. The model is integrated using the finite volume dynamical core at 1.9° × 2.5° horizontal resolution in latitude and longitude, respectively, with 26 vertical levels. We used the subgrid scale physics from CAM4, including the Zhang-McFarlane deep convection scheme⁴ and the Hack shallow convection scheme⁵. We prescribed an orbital eccentricity and obliquity of zero in the parameterizations for radiative transfer, thereby eliminating the seasonal cycle, but the details of radiative transfer have a relatively minor effect on solutions due to our use of prescribed SST.

Computation of the vertically integrated energy flux divergence is performed using data from the last nine years of a 10-year integration. We use the advective form of the energy equation, approximated as the time mean moist static energy budget,

$$(1) \quad \langle \mathbf{u} \cdot \nabla(c_p T + L_v q) \rangle + \left\langle \omega \frac{\partial h}{\partial p} \right\rangle = E + H + R$$

SUPP. INFORMATION: REGIONAL ENERGY BUDGET CONTROL OF THE ITCZ

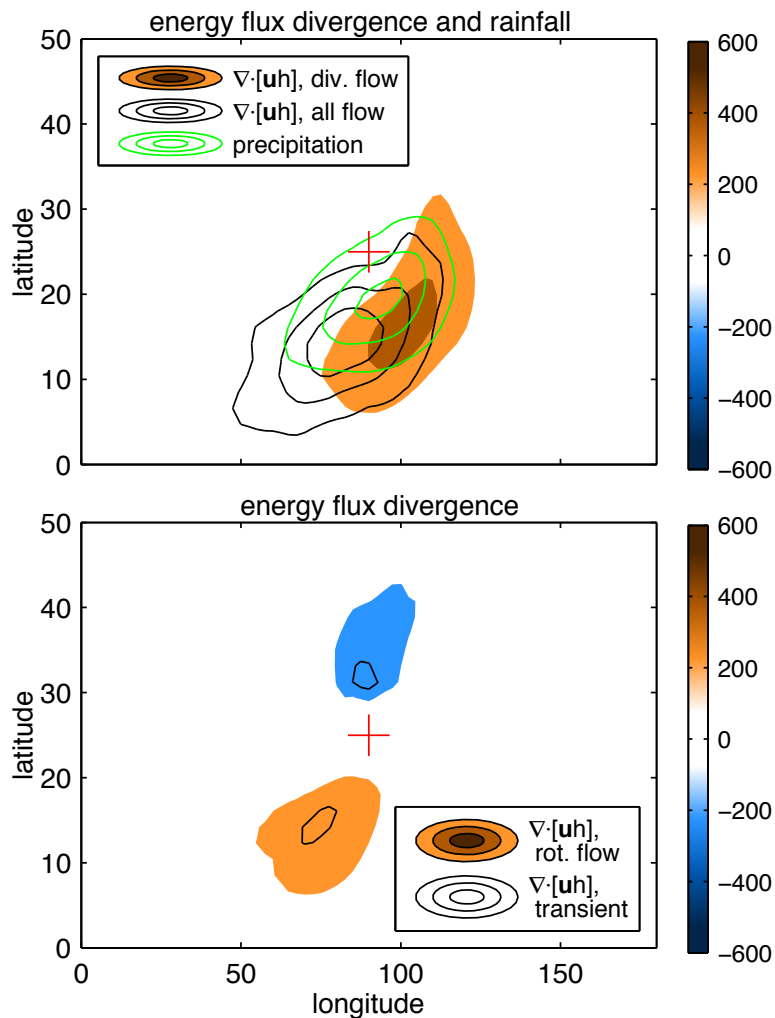
where \mathbf{u} is horizontal velocity, ω is vertical velocity, c_p is specific heat at constant pressure, T is temperature, L_v is the latent heat of vaporization, q is specific humidity, and E , H , and R are the net fluxes of latent heat, sensible heat, and radiative energy through the top and bottom boundaries of the atmosphere. Brackets denote a pressure-weighted vertical integral from surface pressure to the top of the model. The moist static energy $h = c_p T + L_v q + \Phi$ appears in the term representing vertical energy advection, but the geopotential Φ is omitted from the horizontal advection term, consistent with the primitive equations⁶; this form of the moist static energy equation has been used in other studies of tropical atmospheric dynamics⁷. The left side of equation (1) is equal to the divergence of the vertically integrated atmospheric energy flux, while the right side represents the column-integrated sources of moist static energy. We make all computations in the native model vertical coordinate (on η levels) and convert horizontal gradients to pressure coordinates via a standard transformation⁸ for use in equation (1), although this coordinate transformation makes little difference since η and pressure surfaces are nearly parallel due to the lack of orography.

We calculate the vertically integrated atmospheric energy flux convergence accomplished by the total flow, by the time mean flow, and by transient anomalies to that time mean flow. First, we use 3-hourly samples of the model state to calculate each term on the left-hand side of equation (1), then average in time over 9 years. This is done only to confirm that the budget residual is acceptably small: its magnitude is 10% or less of the column-integrated energy source in the region of heavy rainfall. Our main task is using time mean values of T , q , h , \mathbf{u} , and ω to calculate the advective terms, which together give the atmospheric energy flux divergence produced by the time mean flow. After calculating the flux divergence produced by the total time mean flow, we decompose the time mean \mathbf{u} into a horizontally divergent component \mathbf{u}_x and a rotational component \mathbf{u}_ψ . These time mean divergent and rotational winds are then used with the time mean T , q , h , and ω in the left hand side of equation (1) to obtain the vertically integrated energy flux divergence produced by the time mean divergent flow and the time mean rotational flow. To be clear, the energy flux divergence by the time mean divergent wind consists of the sum of horizontal advection by the time mean divergent wind and vertical advection by the time mean flow, while energy flux divergence by the time mean rotational flow consists only of horizontal advection by the time mean rotational wind. The energy flux divergence by transients are computed as a residual by taking the right side of equation (1) and subtracting the energy flux divergence produced by the total time mean flow. Because our energy budget has a small residual, this yields a transient contribution similar to that obtained by explicit calculation from 3-hourly samples of the model state.

1.2. Results. Heavy rainfall (green contours in Supplementary Fig. 3a) occurs just south of the SST maximum, similar to the way that peak rainfall is centered just south of the maximum upper-tropospheric temperature and low-level moist static energy in observed monsoons⁹. This precipitation maximum is thus our idealized analogue of the regional rainfall maxima that occur in monsoon regions. There is strong subsidence and near zero precipitation west of the SST maximum, consistent with previous analytical and numerical solutions to the Gill model^{2;3}.

The total circulation diverges energy away from the precipitation maximum at a rate that peaks at about 600 W m^{-2} and is equal to the rate that energy is input to

SUPP. INFORMATION: REGIONAL ENERGY BUDGET CONTROL OF THE ITCZ



SUPPLEMENTARY FIGURE 3. Association of rainfall with various components of the total atmospheric energy flux divergence in an idealized model. a) time mean precipitation (green contours, interval 15 mm day⁻¹ starting at 15 mm day⁻¹), total energy flux divergence (black contours), and the energy flux divergence produced by the time mean divergent wind (color shading). b) Energy flux divergence produced by the time mean rotational wind (color shading) and by transient motions (black contours). Red cross marks the center of the SST maximum and interval for all energy flux divergence contours is 150 W m⁻².

the atmosphere by surface enthalpy fluxes and radiation. The largest contribution to the total energy flux divergence generally comes from the divergent part of the time mean flow (compare black contours and color shading in Supplementary

SUPP. INFORMATION: REGIONAL ENERGY BUDGET CONTROL OF THE ITCZ

Fig. 3a). The rotational component of the time mean flow produces energy flux divergence with a peak magnitude of about one-third of the total, and the flux divergence produced by transients is even smaller (Supplementary Fig. 3b). There are regions where the rotational flow and transients together produce the majority of the total energy flux divergence, such as southwest of the SST maximum, but the contribution from the divergent wind can be seen to dominate in a bulk sense when one integrates over all regions of positive energy flux divergence (Supplementary Table 1).

This confirms that the divergent part of the time mean flow, which is associated with nearly all tropical and subtropical rainfall, produces the majority of the divergent AET, so one can indeed think of the regional ITCZ as being strongly associated with the regional vertically integrated energy flux divergence. It is possible that *perturbations* to the divergent AET will be dominated by perturbations in rotational flow or in transients that are not associated with time mean rainfall, but this is a subtlety that we leave for future work; results presented in the main text suggest that this is not the case for our mid-Holocene case study.

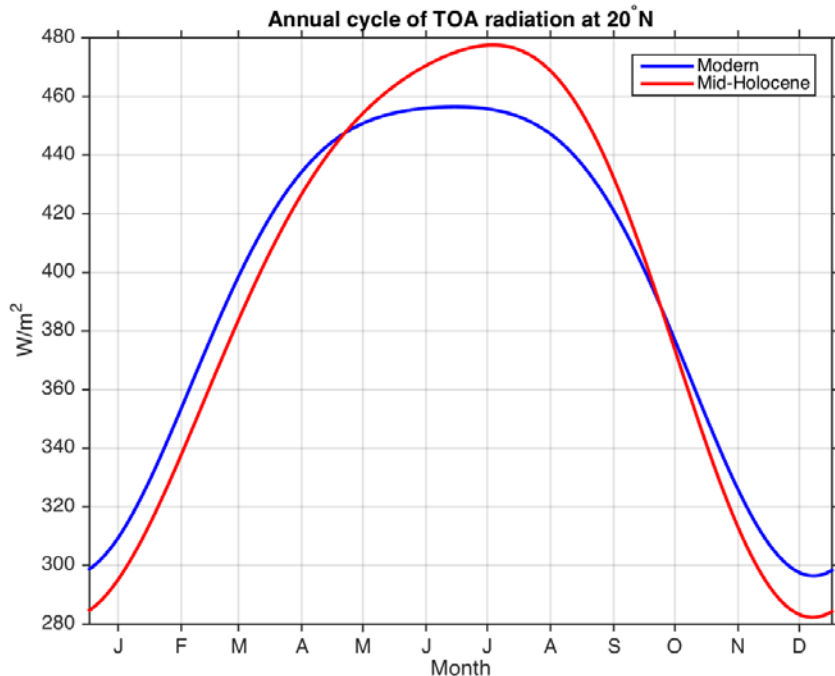
SUPPLEMENTARY TABLE 1. Horizontally integrated positive atmospheric energy flux divergence in our numerical “Gill model”. The energy flux divergence produced by each of the listed wind components is horizontally integrated in a global domain over all regions where the flux divergence produced by that wind component is positive.

Component	Global integral
All winds	6.5 PW
Divergent time mean wind	6.2 PW
Rotational time mean wind	4.4 PW
Transient wind anomalies	3.2 PW

SUPP. INFORMATION: REGIONAL ENERGY BUDGET CONTROL OF THE ITCZ

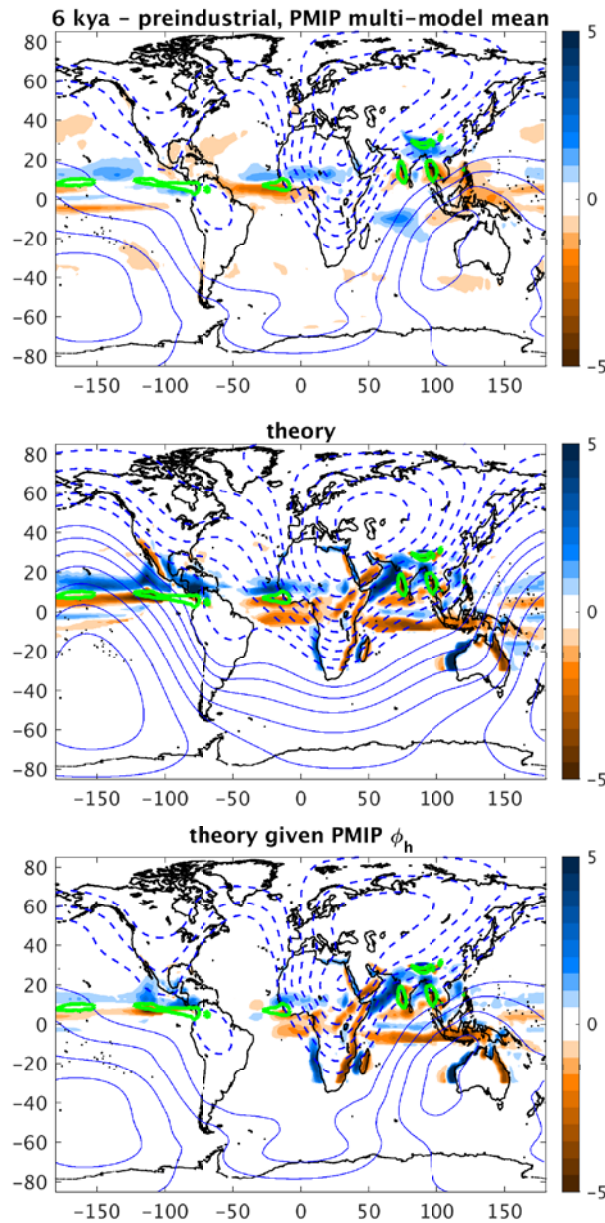
SUPPLEMENTARY TABLE 2. PMIP3 models analyzed and some of their characteristics. “Type” indicates whether the model consists of coupled ocean-atmosphere (OA) components or coupled ocean-atmosphere-carbon cycle (OAC) components.

Model name	Atmospheric resolution (lat × lon × levels)	Type	Reference
CCSM4	0.9° × 1.25° × 26	OA	Gent et al. (2011) ¹⁰
FGOALS-G2	2.8° × 2.8° × 26	OA	Li et al. (2013) ¹¹
MPI-ESM-P	1.9° × 1.9° × 25	OA	Giorgetta et al. (2013) ¹²
MIROC-ESM	2.8° × 2.8° × 80	OAC	Sueyoshi et al. (2013) ¹³



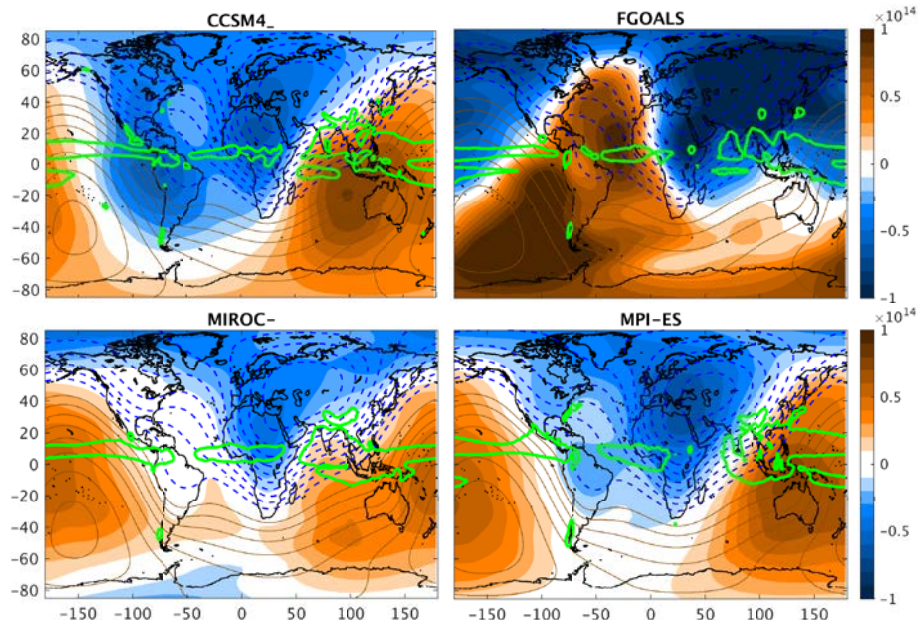
SUPPLEMENTARY FIGURE 4. Annual cycle of solar radiation incident at top of the atmosphere at 20°N during modern times (blue) and during the Mid-Holocene 6000 years ago (red). Grid lines are drawn at midpoint (15th day) of each month. Data from Berger 1978¹⁴.

SUPP. INFORMATION: REGIONAL ENERGY BUDGET CONTROL OF THE ITCZ



SUPPLEMENTARY FIGURE 5. Same as left panels of Fig. 3 of main text but with color shading showing precipitation minus surface evapotranspiration ($P - E$) instead of precipitation. The green contour marks the 6 mm day^{-1} isoline of $P - E$.

SUPP. INFORMATION: REGIONAL ENERGY BUDGET CONTROL OF THE ITCZ



SUPPLEMENTARY FIGURE 6. Energy flux potential response to mid-Holocene forcing in individual models. Color shading shows the model-simulated anomalous energy flux potential and contours show the theoretical prediction of the anomalous energy flux potential, with all contour intervals 0.01 PW. Green contour marks the 6 mm day^{-1} isoline of precipitation. All quantities are May-Sept. climatological means.

SUPP. INFORMATION: REGIONAL ENERGY BUDGET CONTROL OF THE ITCZ

REFERENCES

- [1] Seager, R. & Henderson, N. Diagnostic computation of moisture budgets in the ERA-interim reanalysis with reference to analysis of CMIP-archived atmospheric model data. *J. Clim.* **26**, 7876–7901 (2013).
- [2] Gill, A. E. Some simple solutions for heat-induced tropical circulation. *Q. J. R. Meteorol. Soc.* **106**, 447–462 (1980).
- [3] Rodwell, M. J. & Hoskins, B. J. Monsoons and the dynamics of deserts. *Q. J. R. Meteorol. Soc.* **122**, 1385–1404 (1996).
- [4] Zhang, G. & McFarlane, N. A. Role of convective scale momentum transport in climate simulation. *J. Geophys. Res.* **100**, 1417–1426 (1995).
- [5] Hack, J. J. Parameterization of moist convection in the National Center for Atmospheric Research community climate model (CCM2). *J. Geophys. Res.* **99**, 5551 (1994).
- [6] Neelin, J. D. Moist dynamics of tropical convection zones in monsoons, teleconnections, and global warming. *Glob. Circ. Atmos.* 267–301 (2007).
- [7] Sobel, A., Wang, S. & Kim, D. Moist static energy budget of the MJO during DYNAMO. *J. Atmos. Sci.* **71**, 4276–4291 (2014).
- [8] Haltiner, G. J. & Williams, R. T. *Numerical prediction and dynamic meteorology*, vol. 2 (Wiley New York, 1980).
- [9] Nie, J., Boos, W. R. & Kuang, Z. Observational evaluation of a convective quasi-equilibrium view of monsoons. *J. Clim.* **23**, 4416–4428 (2010).
- [10] Gent, P. R. *et al.* The Community Climate System Model version 4. *J. Clim.* **24**, 4973–4991 (2011).
- [11] Li, L. *et al.* The Flexible Global Ocean-Atmosphere-Land System model, grid-point version 2: FGOALS-g2. *Adv. Atmos. Sci.* **30**, 543–560 (2013).
- [12] Giorgetta, M. A. *et al.* Climate and carbon cycle changes from 1850 to 2100 in MPI-ESM simulations for the coupled model intercomparison project phase 5. *J. Adv. Model. Earth Syst.* **5**, 572–597 (2013).
- [13] Sueyoshi, T. *et al.* Set-up of the PMIP3 paleoclimate experiments conducted using an Earth system model, MIROC-ESM. *Geosci. Model Dev.* **6**, 819–836 (2013).
- [14] Berger, A. L. Long-term variations of caloric insolation from the Earth's orbital elements. *Quat. Res.* **9**, 139–167 (1978).